INTERLAMINAR DAMAGE DETECTION IN COMPOSITE ELEMENTS BY MEANS OF OPTICAL FIBRE SENSORS

P. Bettini[1]*, A. Airoldi[1], P. Bogotto[1], T. Loutas[2]
[1]Dept. of Aerospace Science and Technology, Politecnico di Milano
Via La Masa 34, 20156 – Milano – ITALY
[2]Dept. of Mechanical Engineering and Aeronautics, University of Patras, Greece

Abstract

The interest of aerospace industry about SHM is continuously increasing and many studies are conducted to develop new reliable techniques. Monitoring the health of a structure is essential to prevent failure and improve maintenance activities. This work is aimed at assessing the capability of detecting the outliers originated by interlaminar damages in a relatively bulk composite element, which is a representative component of modern composite structural solution. At first, manufacturing activities are presented with particular attention to the technological issues related to the integration of FO sensors inside laminates. DTG (Draw Tower Gratings) arrays with a configuration reproducing long chirped sensors are embedded and located near three different artificial delaminations. A reference undamaged zone is also monitored in the same way. By using a numerical model of DTGs capable of simulating their acquired spectral response, a new originally developed code is adopted to retrieve the strain field applied along gauge section. Position and size of sensors network and defects are designed by means of a FE analysis of the composite component. Changes in the strain field due to the presence of the defects are evidenced, highlighted, and evaluated by comparing such strain field with the reference one both in numerical models and experiments.

1. INTRODUCTION

Through Fiber Bragg gratings (FBG) carried by optical fibers, local values of strain, stress, temperature, moisture and chemicals concentration can be measured, being immune from electro-magnetic jamming. This technology provides the possibility of developing and implementing sensor networks with different densities that can be applied to structures with different purposes. In modern composite structural components, such aspect assumes a paramount importance, since damage development must be considered along all the component life, including technological defects, damage occurred due to impacts at various energy levels, damage onset and propagations due to fatigue, environmental effects, and difficultly predictable load levels and responses due to aging and interactions with other structural parts.

Indeed, Health Monitoring System (HMS) based on optical fibres have a large potential for radical innovations in the design of composite structural architectures and in the development of highly efficient maintenance procedures for aerospace structures [1]. However, the works presented in literature indicate that a very high density of sensors is typically required for applications oriented at the detection of sub-critical damages, which are also more efficiently performed by embedding optical fibres (OF) into composite laminates to detect internal strain states [2-4]. Therefore, the design of a monitoring system must be performed by knowing with accuracy the signatures of damage on the strain fields, thus providing fundamental information regarding the possibility of detecting sub-critical damages with a given sensor density. Accordingly, the design of SHM systems must require the capability of predicting with adequate accuracy the evolution of strain fields during crack propagation [5] and damage detection must rely on the possibility of identifying the outliers with respect to nominal strain fields, which can be reconstructed on structural composite elements by means of relatively coarse sensor network [6]. However, even if SHM is accurately designed, a significant number of sensors maybe required to detect the weak signature induced by delaminations on real-word components [7]. Chains of common FBGs, which can be inscribed on the same optical fiber exploiting their multiplexing capability, permit an accurate local strain field reconstruction by interpolating local measurements but the maximum spatial resolution that can be achieved with this solution does not permit an efficient defectiveness detection.

To overcome this issue a new type of quasi-distributed sensors, called Draw Tower Grating [8], were tested in this work. DTGs are more considerably strength, reliable and have less unit cost thanks to an innovative technique capable to inscribe the gratings before the coating deposition, allowing different array configurations and giving the possibility to produce different combinations of spatial resolution and spectral reflectivity. As the chirped gratings, these sensors can exploit a one-to-one correspondence between the position of a singular grating along the optical fibre and the position of its reflected peak in the spectrum domain. With respect to standard chirped, DTGs can achieve much greater gage length maintaining an optimal spatial resolution along the entire monitored region. Among the possible configurations, the SPAtial Discontinuity and SPEctral Continuity has proved to be the most suitable solution for local monitoring and strain field reconstruction [9]. Spectral response of this configuration is similar to a chirped spectrum and it can be obtained by tuning the amount of light, reflected from each grating, to be partially overlapped (l_{Bi}-l_{Bi+1}<FWHM). Due to the continuity in the shape of the spectrum the peaks tracking technique cannot be used and a numerical tool is needed to retrieve the strain field from changes of the spectrum shape.

After having applied a numerical model able to simulate the spectral response of a grating subjected to a generic strain profile (*direct problem*), a genetic algorithm and an optimization procedure can be implemented to find the strain profile minimizing the difference between simulated and experimental spectra (*inverse problem*) [10]

Algorithms proposed by Bettini et al. [9] permitted to well reconstruct both linear strain with gradient change and quasi-quadratic strain profile but the resolution of the inverse problem was very time expensive procedure and it is not possible to implement the technique in real time architectures. To overcome this issue, a faster algorithm based on a new iterative procedure is presented in this paper. New algorithm was set and validated using real data coming from previous experimental test. After having compared new results with those obtained with the old procedure, the new approach was applied on a C-shaped spar element in which artificial defects were produced to evaluate damage detection capabilities of such SHM System.

2. DESIGN OF AN APPLICATION CASE FOR SHM SYSTEM

It is well known that, under structural loading, the presence of a damage induces a variation in the local strain distribution, due to the variation of load path. As a consequence, the damage itself can be detected by comparing such altered strain distribution with the strain field affecting the same un-damaged structure. The main drawback of such a procedure resides in the intrinsically *local* nature of damage-induced strain anomalies, which makes damages only detectable in vicinity of strain sensors. As a matter of fact, this does not represent a real hindrance, since structural *hot-spots* can be preliminarily pointed out through FEM analysis. On the other hand, while numerical predictions are generally accurate and straightforward, experimental results may be affected by noise, loading/constraining imperfection and production tolerances. So, direct comparison may result impracticable. An alternative approach makes use of statistical methods, according to which the outcomes of different sensors at different times belong to a single statistical population, provided the measurements are normalized for filtering the effects of load time-variation.

However, the strain field in many structural components is expected to present a smoothly varying distributions in the zones far from the application of concentrated loads. Such aspect can be exploited to detect anomalies that indicate a local alteration with respect to a smooth nominal solution. An example of such approach can be found in [11,12], where an algorithm was devised to identify failures in bonded junction. Another method can be based on the availability of reconstructed strain fields, which can be obtained by means of different methods based on the acquisition of local strains and the application of FE-based techniques [6].

Whichever method is suggested to detect the anomalies, a preliminary evaluation of the effects of damage on the local strain field is required to design the SHM system. In particular, the effects on strain distribution induced by the introduction of defects in components that are representative of modern aerospace composite structure must be investigated.

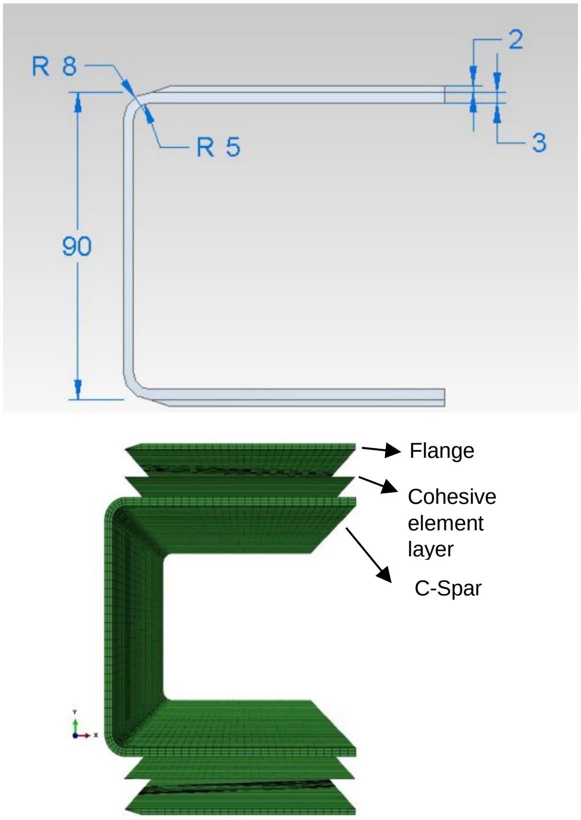

Figure 1: Flanged C-shaped spar considered for damage detection.

To investigate and validate the method, a C-shaped carbon/epoxy wing spar was assumed and modelled as test-bed. The spar was manufacturing by using an homogeneous lay-up of carbon-reinforced plies but two flanges were added on top and bottom surfaces to modify the properties of the web and of the caps of the spar (see Figure1).

The C-shaped original spar consists of 15 plies; its stacking sequence is made of 63% $[45°]_{fabric}$, 25% $[0°]_{unidirectional}$ and 12% $[90°]_{unidirectional}$. Each additional flange consists of 10 plies, whose lamination includes 58% $[0°]_{unidirectional}$, 21% $[0°]_{fabric}$ and 21% $[45°]_{fabric}$. The design of the component was carried out by developing a FE model, where the C-shaped spar and the additional flanges were modelled by using a solid laminated elements and joined together through a layer of cohesive elements, inside which delaminations were modelled by attributing zero stiffness. The component was subjected to a three-point-bending-like loading condition. To analyse different damage scenarios, different sizes (Table 1) of the same delamination (Figure 2) have been considered.

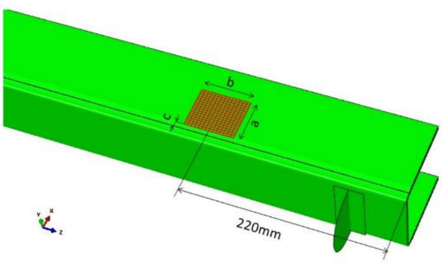

Figure 2: Scheme of delaminations position and size.

Damage configuration	a (mm)	b (mm)	c (mm)	A (mm^2)
#C1	48	56	0	2688
#C2	48	72	0	3456
#C3	48	56	6	2688
#C4	48	72	6	3456
#C5	69	72	6	4968
#C6	48	72	36	3672

Table 1: Delaminations position and size.

Strains were evaluated along paths (which correspond to the optical fibres carrying FBGs), whose traces in the section of the model are shown in Figure 3. The model of the spar was subject to a three-point bending load condition and typical strain distribution curves, for every combination of damage size and measuring path were obtained, showing that distribution have different degree of sensitivity along different paths and considering different damage sizes. The examples reported in (Figure 4) show that the alteration of the strain distribution along external paths, like paths 1 and 9, is characterized by a moderate amplitude distributed along an appreciable span length. However, alteration is very sensitive to the position of the path with respect to the damage location, since path 1 shows very limited variation with respect to the undamaged conditions.

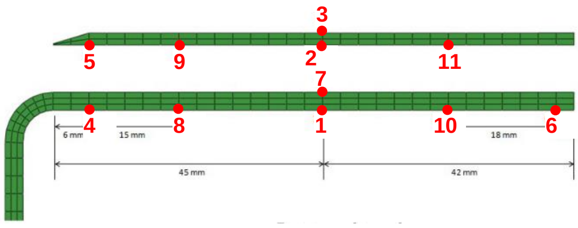

Figure 3: Measurement points of strain field in the delamination zone.

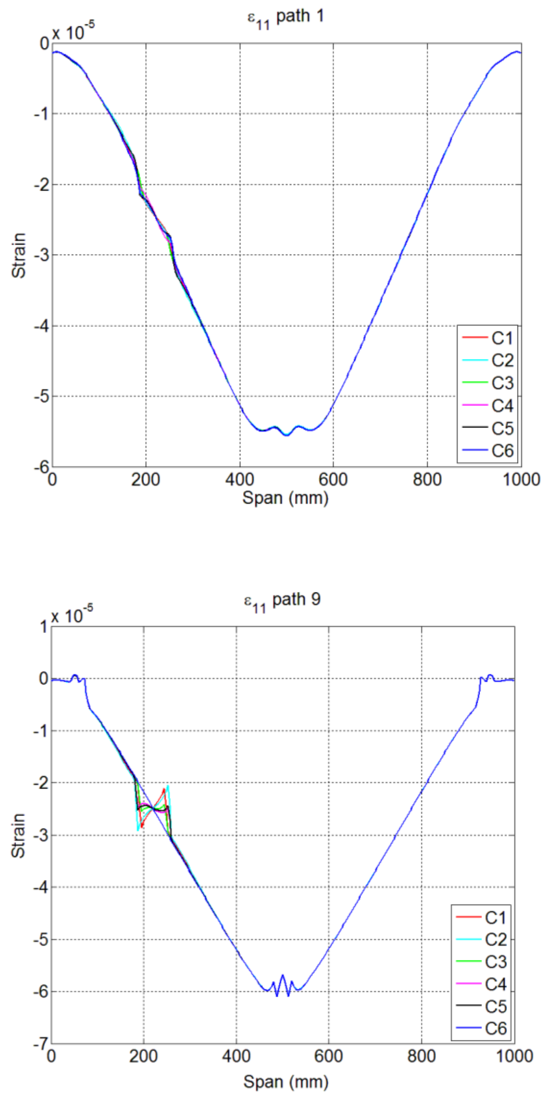

Figure 4: Strain distribution along different paths for different damage scenarios.

The alteration along internal paths located in the flange, two plies above the layer of cohesive elements, are characterised by higher amplitudes, though they are extended over a lower span. Moreover, internal paths appear less sensitive to damage localization.

Once completed such a screening procedure, a damages/paths the configuration shown in Figure 5 was defined to experimentally assess the damage detection capability of different methods.

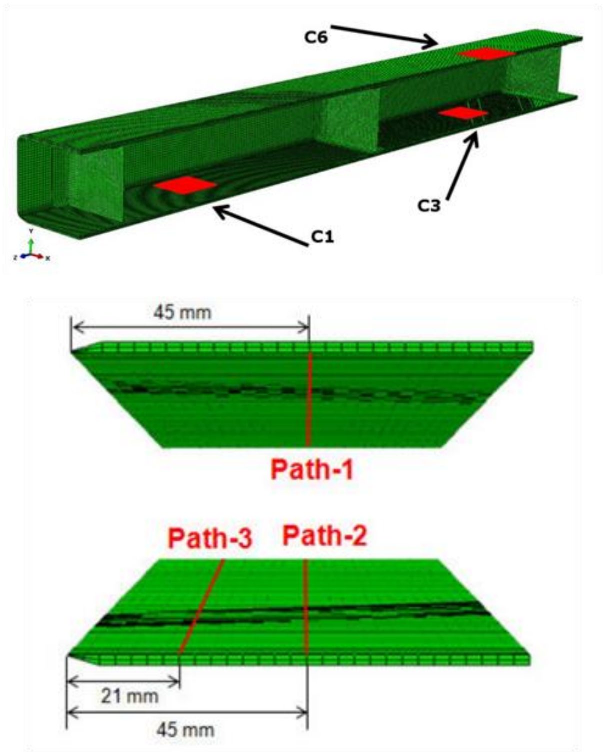

Figure 5: Final configuration of damage scenarios and damage detection path.

	Lay-up #1	Lay-up #2	Lay-up #4
C-Spar			
FB 45°	50%	100%	41.6%
UD 0°	25%	-	41.6%
UD 90°	25%	-	16.8%
Flange			
FB 45°	50%	-	15%
UD 0°	25%	100%	12.5%
UD 90°	25%	-	62.5%

Table 2: Sensitivity of damage detectability to different lay-ups.

It is worth mentioning that the design phase of the experiments pointed out that a strong influence is exerted by the stacking sequence on damage detectability has to be evaluated. Comparing the four laminations reported in Table 2 it appears that the more spar and flanges laminations differ, the more easily damage can be detected (see typical curves shown in Figure 6).

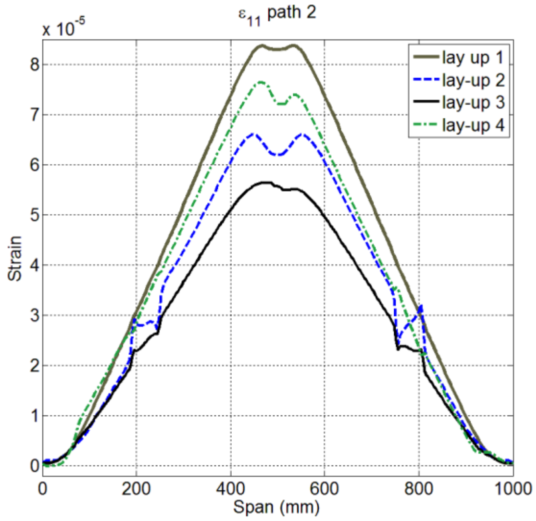

Figure 6: Sensitivity of damage detectability to different lay-ups.

3. MANUFACTURING AND PHYSICAL INTEGRATION OF SHM SYSTEM

The technological demonstrator was manufactured by autoclave moulding. According to the design, the production consisted in two phases. The first one was devoted to cure a 1 m long C-shaped spar while in the second phase a co-bonding cycle was done to add the two external flanges. Artificial defects made of properly sized PTFE patches were inserted at the interface between the components. Optical fibers were embedded during lamination between the 2nd and 3rd ply in positions corresponding to the damage detection paths. The sensor's architecture was composed by two DTG arrays whose configuration and main characteristics are summarized in Table 3.

Flange	UPPER	LOWER
Array length (mm)	100	200
N° FBG	10	20
FBG length (mm)°	3	3
Defect size (mm·mm)	56x48	72x48
FBGs pitch (mm)	10	10

Table 3: Characteristics of artificial defects and DTG arrays embedded in the spar.

Sketches reporting relative positions between sensors and defects are shown in the Figure 7.

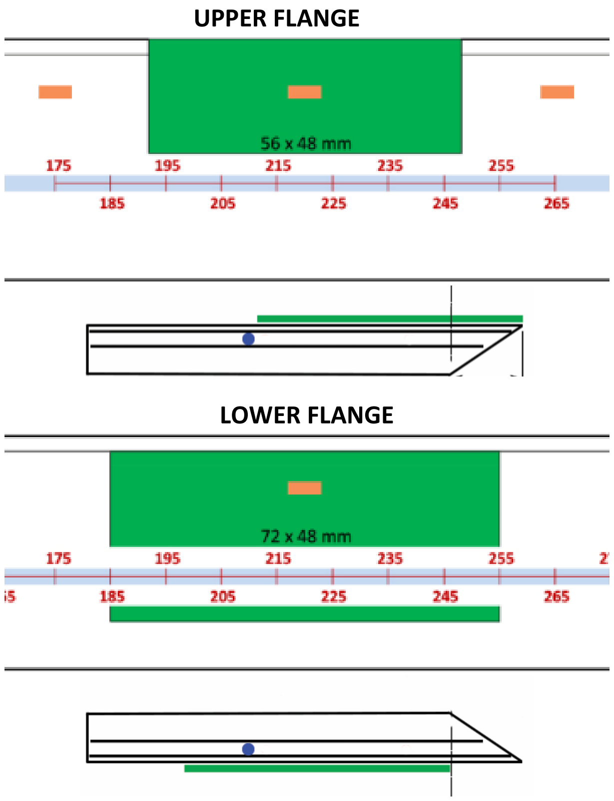

Figure 7: Measurement points of strain field in the delamination zone.

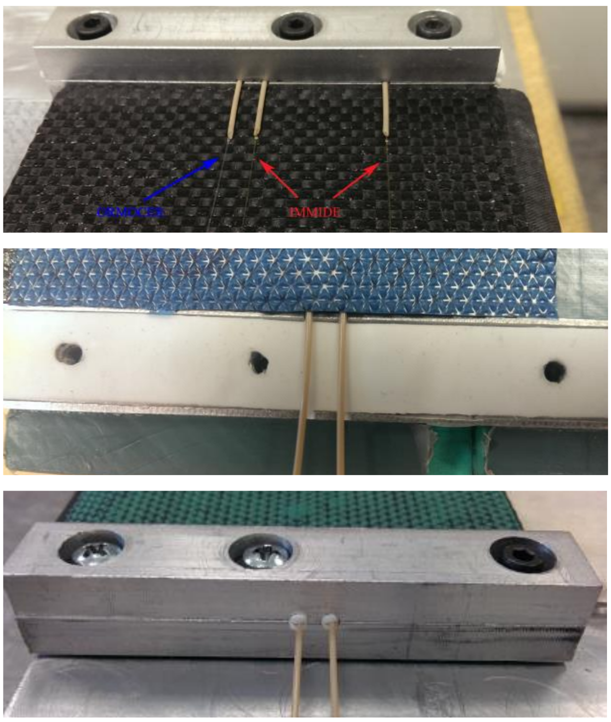

Figure 8: Metallic dam provided with a special by-pass for optical fibres protection at the exit from the mould.

The smallest patch was inserted in the upper flange where the optical fibre was placed a part of the defect. Differently, the sensor was co-located with the defect on the lower side. Orange spots indicate reference strain gauges installed on the external surfaces.

From the technological point of view, the main difficulty was the protection of the optical fibres exiting from the laminate that required designing a devoted tool.

Figure 8 shows the by-pass developed to permit the passage of the optical fibres through the dam of the mould, which is needed to block the resin in excess exiting from the laminate during curing cycle. Small PEEK tubes were also used to preserve OF integrity. Optical fibres coming from the by-pass reach a special box that allows the passage of the fibres from the upper side to the lower side (see Figure 9). The adopted solution permitted to maintain optical fibres inside the vacuum bag protecting them also from the curing pressure.

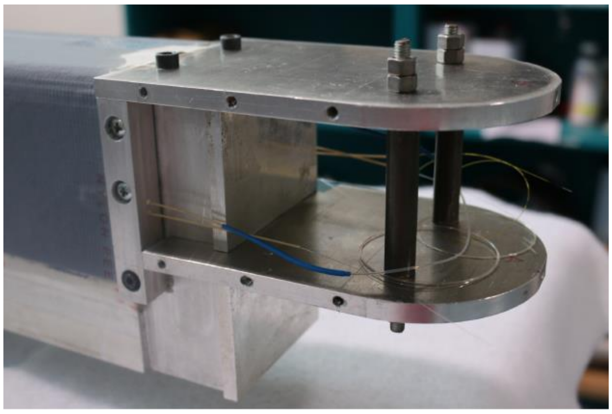

Figure 9: The special box procduced to permit the passage of the OF from the upper side to the lower side.

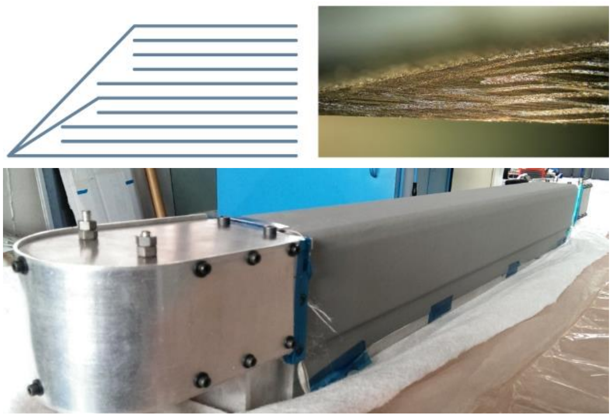

Figure 10: The quasi distributed ply drop-off (top) and the final assembly before curing (bottom).

Finally, figure 10 highlights the quasi-distributed ply drop-off was realized at the edge of the flanges in correspondence of the corners of the C-shaped spar to avoid critical stress concentrations. The elastomeric pad covered the laminate during curing process is also visible in the figure.

4. ALGORITHMS FOR STRAIN RECONSTRUCTION

The first step to develop a strain reconstruction tool consists in the implementation of an algorithm simulating the reflected spectrum of a sensor subject to an arbitrary deformation profile. Common grating simulation techniques are based on the Coupled Mode Theory (CMT), a simplified theory derived from Maxwell's equations [13] that describes light propagation in an optical guide. A broadband light can propagate in the core of the fibre only assuming predefined modes. CMT is represented in Eq. 1.

$$(1) \qquad \boldsymbol{E}_t(x,y,z,t) = \\ = \sum_j \left[A_j(z)e^{i\beta_j z} + B_j(z)e^{-i\beta_j z}\right]\boldsymbol{e}_{jt}(x,y)e^{-i\omega t}$$

where *z* is the axis of the FO and *x, y* are the transverse section coordinates.

For unperturbed waveguide the longitudinal counter-propagating modes are decoupled, $A_j(z)$ and $B_j(z)$ represent the forward and backward mode's amplitude while $\boldsymbol{e}_{jt}(x,y)$ describes the transverse distribution.

When waveguide properties are perturbed, the modes can couple each other, intensifying their amplitude. FBGs represent a perturbation in the core refractive index that couples the modes and generates the reflected spectrum peak. Each peak is tuned, changing the pitch at precise wavelength in accordance with the Bragg's law

$$(2) \qquad \lambda_b = 2\,\pi\,\Lambda$$

where Λ is the grating's pitch, different for every array's FBG.

The behaviour of the light due to FBGs can be described in terms of two modes, one transmitted mode and one reflected mode. Appling the Eq. (1) to a cylindrical single-mode waveguide and rearranging the terms, a new set of first-order differential equations can be obtained:

$$(3) \qquad \begin{cases} \frac{dR(z)}{dz} = i\hat{\sigma}R(z) + ikS(z) \\ \frac{dS(z)}{dz} = -i\hat{\sigma}S(z) - ik^*R(z) \end{cases}$$

where R and S are the transmission and reflection coefficient respectively, while $\hat{\sigma}, k, k^*$ are coupling coefficients. A more detailed mathematical description can be found in [14,15].

In the more general case of non-uniform grating a close form solution is not allowed and a numerical approximation is required to solve the set of equations. Different methods can be performed as Runge-Kutta scheme, Fourier transform or Transfer Matrix Method (TMM) [16].

Past experiences demonstrated the time efficiency of TMM with respect to other numerical methods maintaining the same accuracy. This method requires to subdivide each grating in a number N of sub-gratings smaller enough to approximate each one as constant proprieties grating. Since the analytical solution of Equations (3) are known, the following equations can be written for each subsection:

$$(4) \qquad \begin{bmatrix} R_{i-1} \\ S_{i-1} \end{bmatrix} = \boldsymbol{F}_i \begin{bmatrix} R_i \\ S_i \end{bmatrix} \qquad i = 1{:}\,N$$

where $\boldsymbol{F}_i$ is the 2x2 i-th sub-matrix; more detailed explanations were find in [9]. Once $\boldsymbol{F}_i$ is computed for every sub-grating the transfer matrix for the entire grating F can be obtained multiplying each sub-matrix:

$$(5) \qquad \begin{bmatrix} R_0 \\ S_0 \end{bmatrix} = \boldsymbol{F}_1\boldsymbol{F}_2 \cdots \boldsymbol{F}_i \cdots \boldsymbol{F}_M \begin{bmatrix} R_N \\ S_N \end{bmatrix} = \boldsymbol{F} \begin{bmatrix} R_N \\ S_N \end{bmatrix}$$

Applying boundary conditions $R_0 = 1$ and $S_N = 0$ [14], reflection and transmission amplitudes $r(\lambda)$ and $t(\lambda)$ can be computed for every wavelength; consequently, reflectivity $R = r^2$ and transmission $T = t^2$obtaining the full reflection spectrum.

$$(6) \qquad r(\lambda) = \frac{S_0}{R_0} = \frac{F_{21}}{F_{11}} \qquad t(\lambda) = \frac{R_M}{R_0} = \frac{1}{F_{11}}$$

TMM permits to solve the *direct problem* for every kind of grating and strain profile applied along it. Furthermore, this procedure is essential in the inverse problem resolution's algorithms.

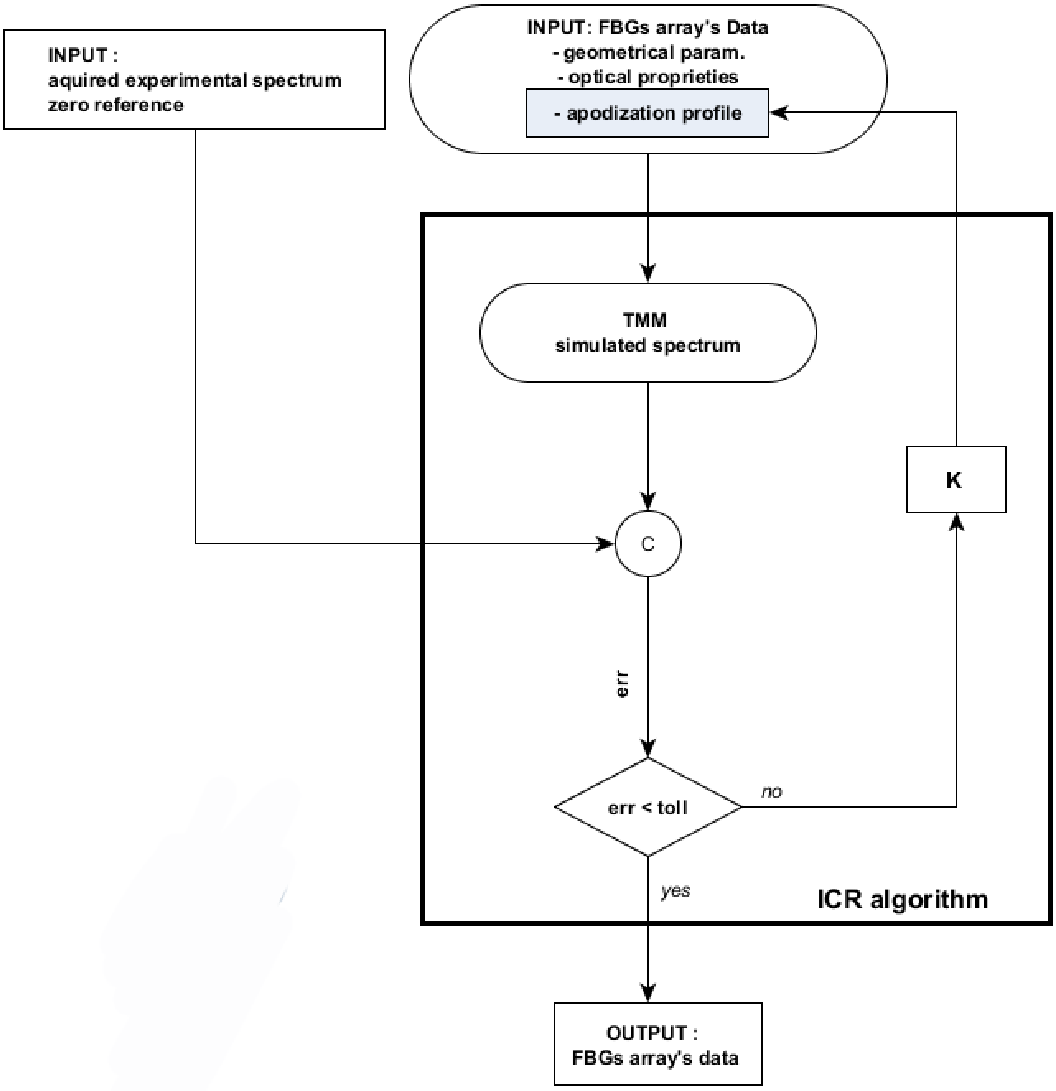

Figure 11: Flowchart of the Initial Condition Reconstruction algorithm.

To reduce computational times, which represent the main limitation of algorithms for strain profile reconstruction developed in the past, a preliminary algorithm devoted to the reconstruction of initial conditions (ICR) was proposed. Inverse problem can then solved by using a devoted procedure named FBGCenter.

4.1. Initial Condition Reconstruction procedure: ICR

Due to grating's imperfections, loss of signal and external perturbation, the real spectrum never matches with the numerical one. In order to avoid the introduction of an error in the strain reconstruction procedure, which can cause the method to be not accurate, this discrepancy has to be avoided.

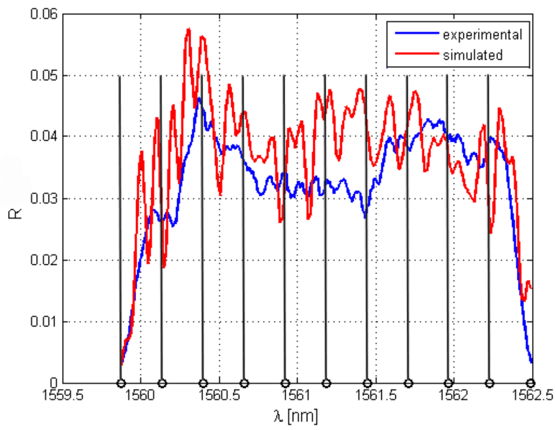

Figure 12: Flowchart of the ICR algorithm.

Under the assumption that each grating has a one-to-one spectrum correspondence and contributes with the same amount of reflected light, the procedure aims to compute a new apodization profile that generates the best matching between acquired and simulated spectrum. Figure 11 shows the flowchart representing the main blocks of ICR procedure.

Input of the procedure are all the sensor's data required to solve the TMM, as the real reference acquired spectrum (normally corresponding to undeformed configuration) and the initial apodization profile guess. C-block in the figure represents the *comparison procedure* between real and computed (TMM) spectrum. As it can be noted in the Figure 12, spectra are divided in M sub-spectrum, with M equal or multiple of the FBGs in the array.

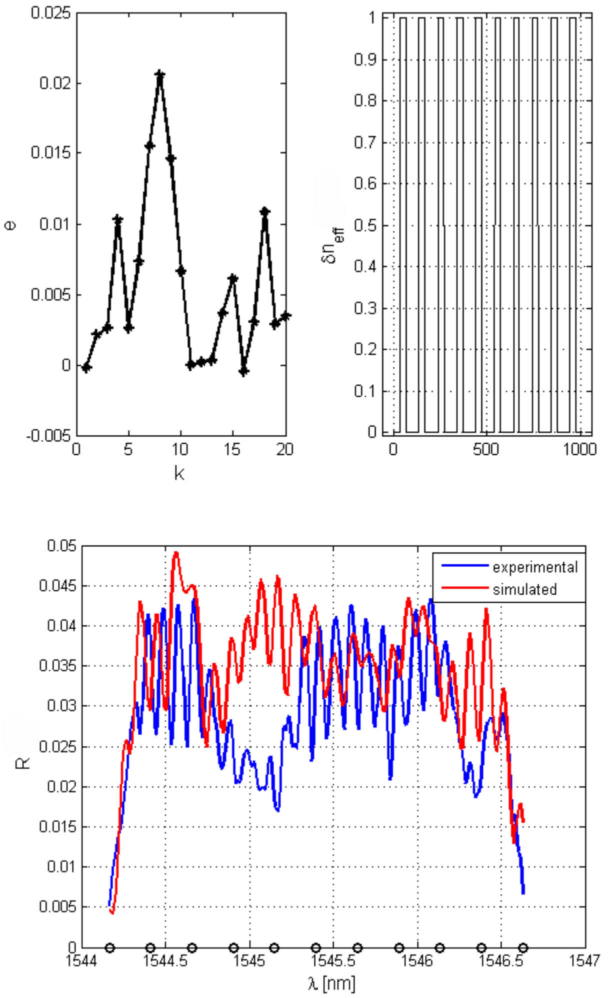

Figure 13: ICR algorithm output at 1st iteration for 10 FBGs array spaD/speC configuration: On the top initial sub-division errors and initial $\Delta\delta n_{eff}$ guess profile.

The output is the error vector **e**, containing the mean value of the amplitude difference between each sub-spectrum where $err = max(\boldsymbol{e})$. If the simulated spectrum with the guess apodization profile is not close enough to the real one, the iteration continues until the convergence is reached (see Figure 13 and Figure 14).

The K-block represents the *apodization control block* and generates the $\Delta\delta \mathrm{n}_{\mathrm{eff}}$ as output. The procedure assumes **K** as a square tridiagonal control matrix. The diagonal terms are the direct control gains whereas the upper and lower diagonal terms take into account for the non-exact correlation between spectral and spatial sub-divisions of the grating.

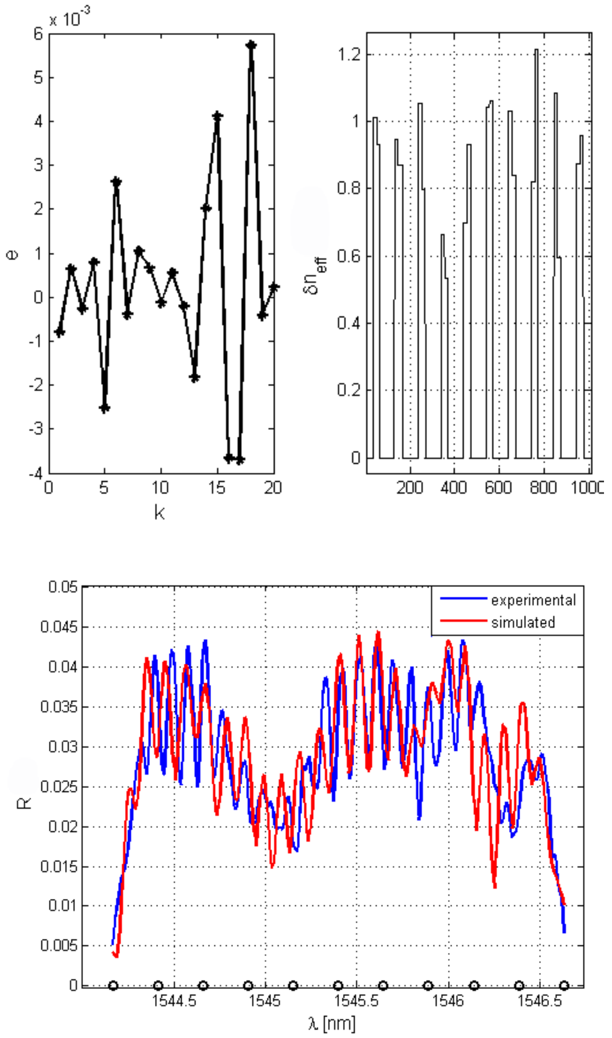

Figure 14: ICR algorithm output at 5th iteration for 10 FBGs array spaD/speC configuration. On the top final sub-division errors and $\Delta\delta n_{eff}$ profile.

.

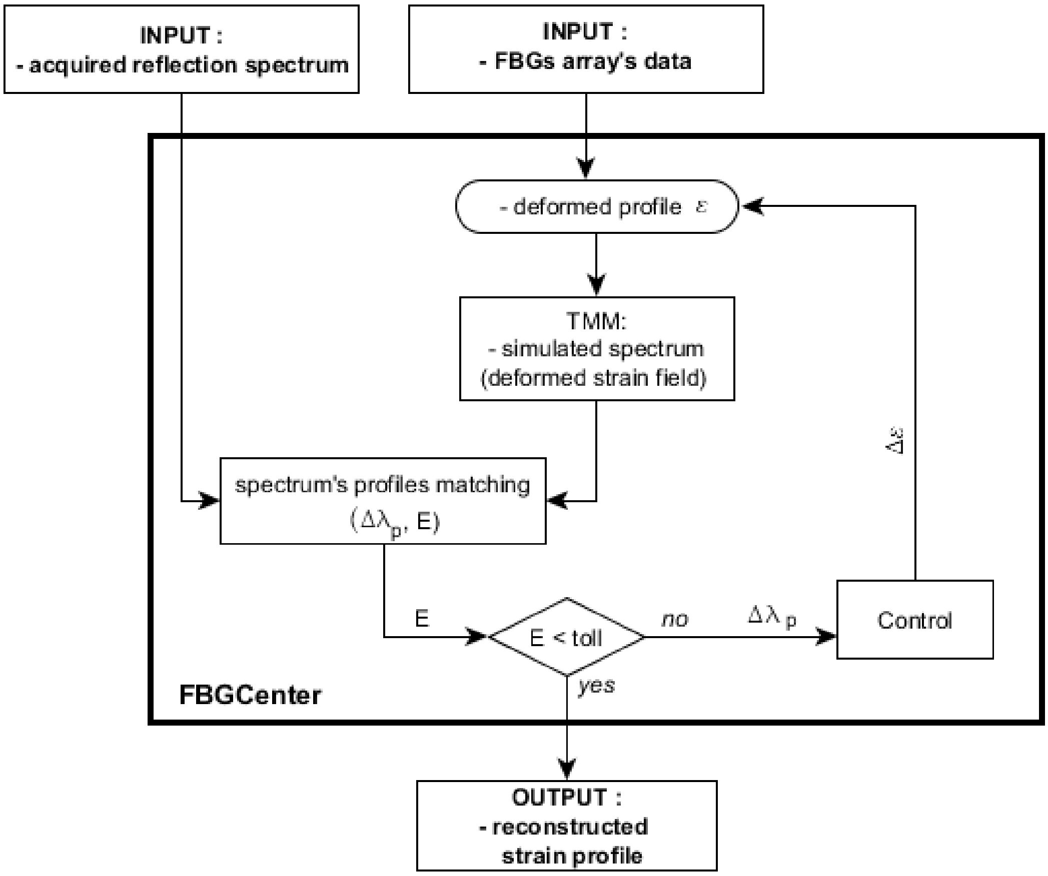

Figure 15: Flowchart of the FBGCenter algorithm for strain reconstruction (inverse problem resolution).

(7) $\Delta n_{eff} = \mathbf{K} \cdot \mathbf{e}$

The procedure represents a simple proportional control method and the correction is carried out as

(8) $\delta n_{eff\ (i+1)} = \delta n_{eff\ (i)} + \Delta\delta n_{eff}$

4.2. Inverse problem resolution: FBGCenter

The sequence of logical operations for strain profile reconstruction implemented in the FBGCenter algorithm is shown in Figure 15. As input, the algorithm needs the sensor's data, the apodization profile previously computed (ICR) and the spectrum acquired in the loaded\deformed configuration. The output of the methods is a vector containing the strain values of N points representing the array FBGs along the FO length, called deformation points (*p.d*). These points also represent the control points of the whole procedure. The core of the FBGCenter algorithm is the *spectrum's profile matching block* devoted to compare the acquired deformed spectrum and the computed one, trying to transduce the information carry by the spectra in strain field acting along the monitoring region. After the definition of the limits in the spectral domain in order to exclude the noise disturb before and after the signal reflected from the sensors, the total area under the spectrum is calculated for both profiles (acquired and simulated): A^A_{tot}; A^S_{tot}. Both spectra are then divided in N sub-spectrum with normalized area equal to $\hat{A}_i$, under the constrain:

(9) $\hat{A}^S_i = \hat{A}^A_i \qquad i = 1\!:\!N$

where $\hat{A}_i = {}^{A_i}\!/_{A_{tot}}$ and $A_i = \int_{\lambda_{i-1}}^{\lambda_i} R(\lambda)\, d\lambda$, and the corresponding centroid is computed λ_{Pi}.

Since the shape of the spectrum is correlated with the strain field along the FO axis, the change of each centroid position indicates a change in the deformation acting along the fibre. Thus, the centroid's difference between each couple of acquired and simulated sub-spectrum (Eq. 10) represents a correspondent difference in terms of deformation between real and simulated strain field.

$$\Delta\lambda_P = \Delta\lambda_P^S - \Delta\lambda_P^A \qquad (10)$$

The vector **E** contains the values of the errors for every N subdivision. The error represents the absolute value of the difference between acquired and computed spectra's values in each division.

The second core of the FBGCenter is the *control block*. The algorithm implemented in this block generates the strain value for each *p.d.* using the information $\Delta\lambda_P$ from the previous matching block (eq.11).

$$\delta\varepsilon_{z\,i}^{m} = \frac{1}{\mathrm{K_m}}\,\Delta\lambda_{P\,i} \qquad i = 1{:}N \qquad (11)$$

where K_m is the usual coefficient to proportionality that describes the drifting of the FBG peak due to mechanical stress.

The vector $\delta\varepsilon_z^m$, which represents the strain value of each deformation point (eq.12), is computed at every iteration *j*, and the final strain field is obtained interpolating these values along the array.

$$\boldsymbol{\varepsilon}_{j+1} = \boldsymbol{\varepsilon}_j + \delta\varepsilon_z^m \qquad (12)$$

Once the deformation profile $\varepsilon(z)$ is computed, these data become the new input for the direct problem procedure until convergence is reached.

4.3. Validation test

Benchmark tests were performed to validate the developed strain reconstruction algorithm.

One DTG array of the same type embedded into the C-shaped spar was bonded to an aluminium beam in order to reproduce to the sensor the following controlled strain profiles by applying it simple loading conditions (see Figure 16): linear strain; linear strain with gradient change; quadratic strain. Red lines indicate the array position.

As example, results obtained for linear strain field are reported in figure 17. In this case 10 p.d. were used as interpolation points. Even if small differences can be noted on the left side and central part of the reconstructed curve, the applied strain profile was correctly reconstructed both in compression and in tension (at the bottom in the figure). Moreover, some discrepancies with respect to the experimental ones are well visible also in the shape of simulated spectrum. Since these discrepancies are located at the first and sixth peak, which correspond to the same zones (left side and central part respectively) of the reconstructed strain profile, this confirms the correct working of the both algorithms.

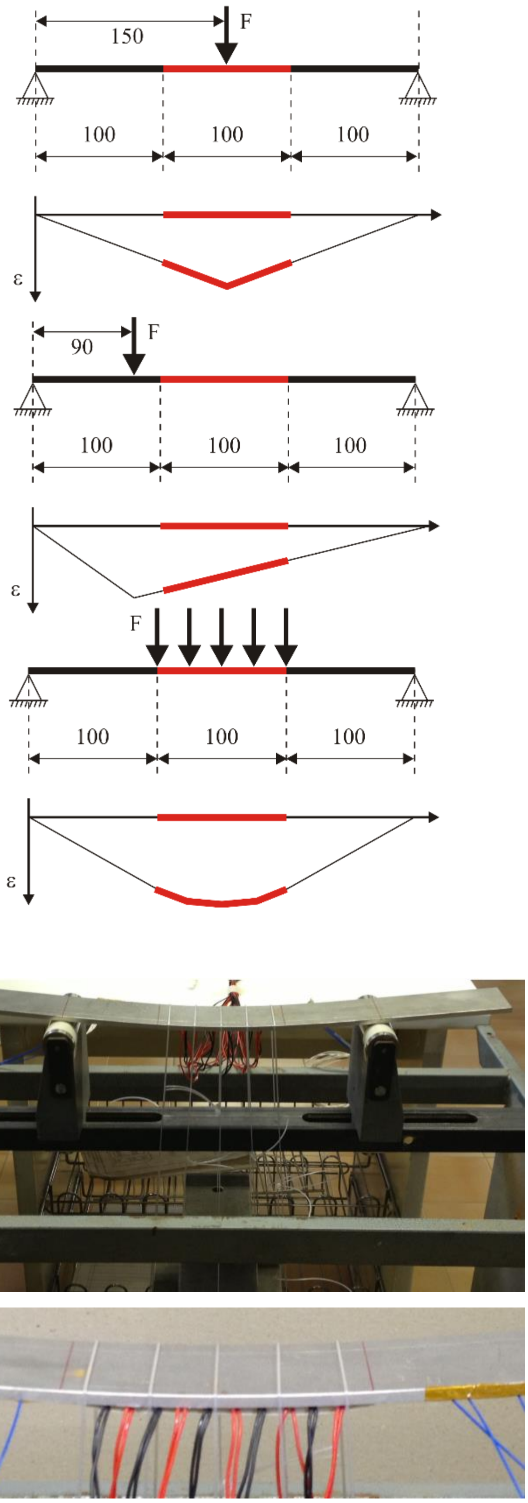

Figure 16: Benchmark tests related to different strain fields produced on DTG array. The quadratic strain profile was obtained by distributing 5 concentrated forces F along the beam (bottom).

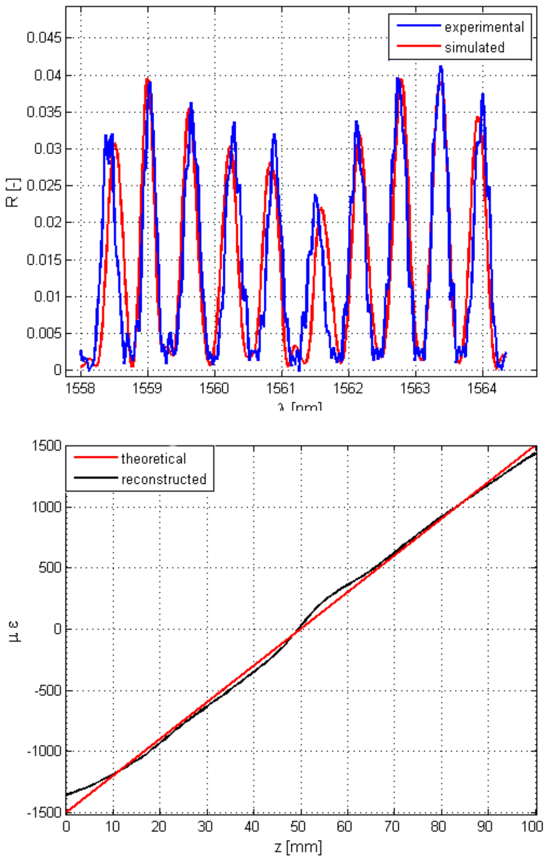

Figure 17: Linear strain profile reconstruction and simulated spectrum with FBGCentre procedure.

5. TESTING AND RESULTS

The C-shaped spar was tested in 3 point bending loading condition. Metallic elements were designed to fix the spar to the testing machine and to apply the loading at shear centre.

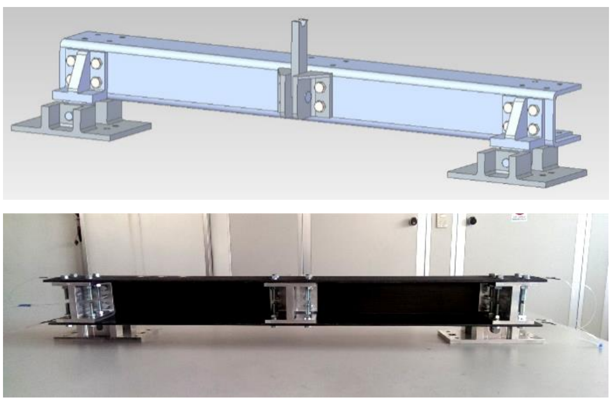

Figure 18: Metallic elements applied to the C-shaped spar.

Figure 19 shows the setup of the test. The exact position of the shear centre was determined by tuning loading application points until no torsion was recorded on the spar. Strain gauges bonded on the surface were also used to drive this tuning.

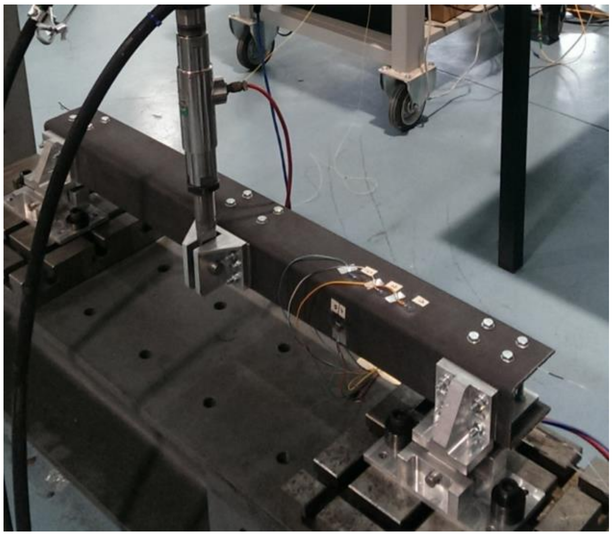

Figure 19: Experimental setup.

The test was conducted in static conditions by applying the force through a servo-hydraulic actuator connected to the central element. The force was increased step by step reaching predefined values (Table 4).

Step	#1	#2	#3	#4
Load F (KN)	0	10	17	22

Table 4: Steps of load applied to C-shaped spar during the 3-point bending test.

Once the force and the acquisition system were stabilized, reflection spectra of the DTG arrays, whose positions are indicated in the Figure 20, were acquired for every loading level. Tunable scanning laser was adopted both as source and data acquisition.

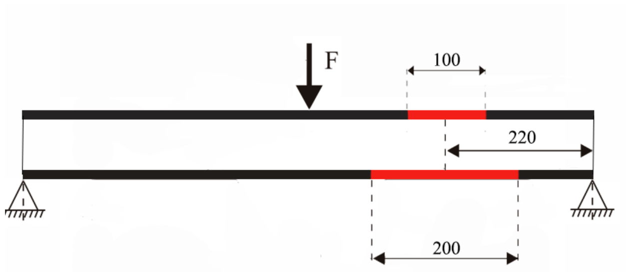

Figure 20: Postion of DTG arrays embedded into C-shaped spar.

Finally, the strain acting along the FO axis under the applied force was reconstructed by using the FBGCenter algorithm.

Many sampling were done for every loading level to guarantee the measurement's repeatability. The reflected spectrum from both the embedded sensors in unloaded spar configuration (F = 0 N) was chosen as initial condition (zero deformation offset) and the ICR algorithm was applied to these spectra. All reconstructed strain fields referred to these two configurations. Figure 21 reports the results obtained at the step 1 in the lower flange. Monitored zone was 200mm long and the defect was located from z≃64 mm to z≃136 mm. On the top of the figure, the simulated spectrum is compared with the real one. The correspondent reconstructed strain field is reported at the bottom.

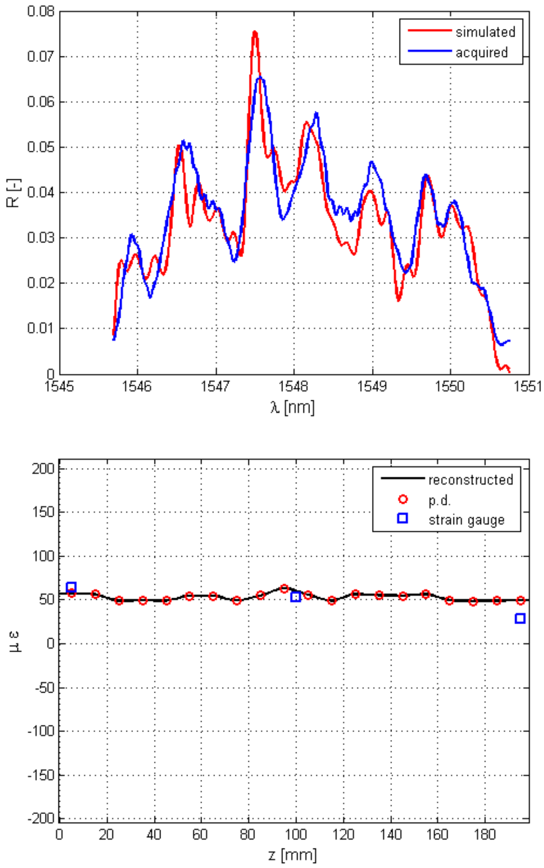

Figure 21: Initial conditions reconstructed in the lower flange.

Simulated and experimental spectra have a good correlation and a constant deformation was retrieved. Since a force F=0 N was applied no deformations were expected. In effect, the obtained values are very small and they were probably caused by residual stress. Anyway, the same strain levels were measured also by SG confirming the adequacy of the method. Strains reconstructed in both the upper and lower flanges at F=17 KN are shown in the figure 22. A discontinuity in the strain field appears around the edges of the artificial delaminations, as expected from numerical activity (see Figure 4). It can be noted that only the left side (z≃30 mm) of the defect is visible in the upper flange, where the small defect was located from z≃22 mm to z≃78 mm. Conversely, the discontinuities are clear visible in both edges of the lower flange where the big defect was placed.

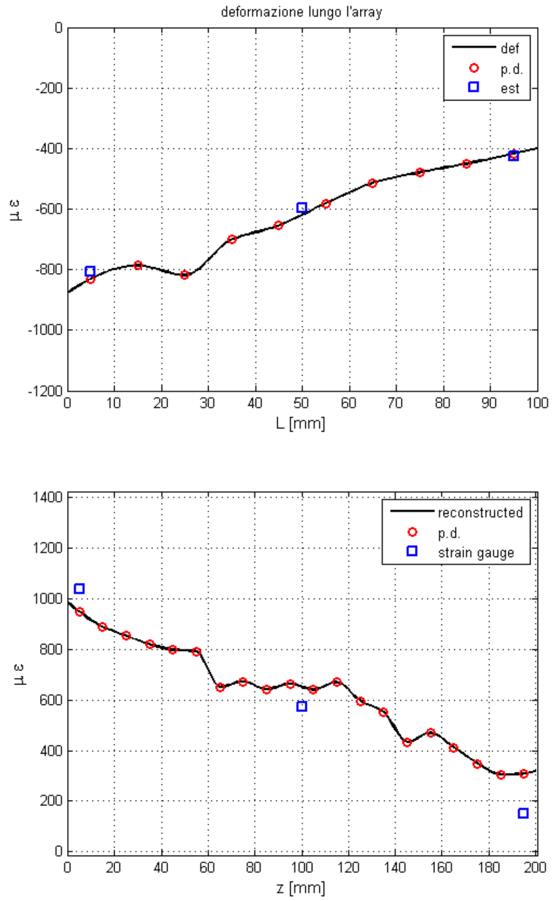

Figure 22: Reconstructed strain in UPPER (top) and LOWER (bottom) flanges under 17 KN.

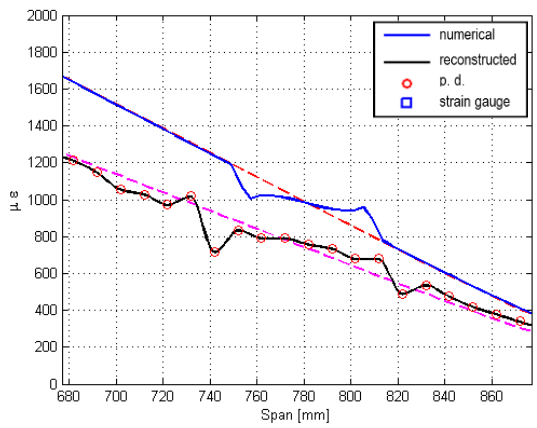

Figure 23: Comparison between reconstructed strain field and FE numerical analysis. Reconstructed strain was obtained at a loading level of 22 KN while FE analysis referes to 25 KN.

By observing the figure 23, a gradient change can be noted between the two discontinuities in the reconstructed strain curve. In particular, a decrease of the gradient was evidenced as a consequence of the presence of a delaminated area. The same behaviour is evidenced also from the numerical curve reported in the graph and related to a FE analysis.

6. CONCLUSIONS

In this work the capability of optical fibre sensors of detecting the outliers originated by interlaminar damages in a relatively bulk composite element was assessed. DTG (Draw Tower Gratings) arrays with a configuration reproducing long chirped sensors were used in combination with a numerical tool to reconstruct the strain profile around two different artificial delaminations. After having physically simulated the sensors (through a model based on CMT), two different algorithms were originally developed to find initial conditions and then to reconstruct the strain profile applied to the sensors. Even if some limitations were highlighted, simple validation tests demonstrated the correct working of this method. Thus, the technique was applied to a C-shaped composite spar reinforced with 2 added flanges representing a real-word bulk component. The design of this technological demonstrator was accomplished by using FE models able to evaluate the influence of the component's delaminations on the strain profile under a like three point bending loading condition. Position and size of the artificial defects, inserted in the laminate to create predefined delaminations, as well the optimal stacking sequence were determined during this preliminary phase, which underlines that the sensitivity of monitoring system and soundness of results are remarkably affected by laminate stacking sequence as well by damage-to-measuring path mutual distance.

Final tests proved the presence of local discontinuities in the strain profile near the edges of delamination area. A change in the strain gradient was also appeared for biggest defects or higher loading levels. Local nature of these discontinuities confirms the limitation of monitoring techniques based on few quasi punctual sensors, like standard FBGs that cannot be susceptible of changes occur far of them.

DTG arrays, here used 200 mm long but potentially available up to meters, can overcame this limitation representing a very interesting sensors type.

Moreover, developed algorithms have been capable to reconstruct small local anomalies in the strain filed demonstrating a good sensitivity and high spatial resolution of the presented technique.

7. AKNOWLEDGEMENTS

The authors wish to thank Optical Sensing Technologies S.r.l. for providing materials and information about DTG arrays. Experimental activity was carried out thanks to the facilities of LAFOS Lab of Politecnico di Milano.

8. REFERENCES

[1] Loutas T.H., Charlaftis P., Airoldi A., Bettini P., Koimtzoglou C., Kostopoulos V., *Reliability of Strain Monitoring of Composite Structures via the Use of Optical Fiber Ribbon Tapes for Structural Health Monitoring Purposes.* Composite Structures 134, 762-771 (2015)

[2] Zhou G., Sim L.M., *Damage detection and assessment in fiber reinforced composite structures with embedded fibre optic sensors-review*. Smart Mater Struct 11,925–39 (2002)

[3] Sala G., Di Landro L., Airoldi A. and Bettini P., *Fibre optic health monitoring for aeronautical applications.* Meccanica 50 (10), 2547-2567 (2015)

[4] Yashiro S., Takeda N., Okabe T. and Sekine H., *A new approach to predict multiple damage states in composite laminates with embedded FBG sensors.* Composite Science and Technology 65, 659-667 (2005)

[5] Airoldi A., Baldi A., Bettini P., Sala G., *Efficient Modelling of Forces and Local Strain Evolution During Delamination of Composite Laminates.* Composites part B - Engineering 72, 137-149 (2015)

[6] Airoldi A., Marelli L., Bettini P., Sala G., Apicella A., Strain Field Reconstruction on Composite Spars Based on the Identification of Equivalent Load Conditions. *Proceedings of SPIE 2017* Portland, OR, USA, 25-29 Mar. 2017

[7] Airoldi A., Bettini P., Belotti P., Loutas T., Koimtzoglou C., Sala G., Design of Health and Usage Monitoring Systems Based on Optical Fibers for Composite Wing Spars. *Proceedings of 34th Conference and the 28th Symposium of the International Committee on Aeronautical Fatigue and Structural Integrity (ICAF),* Helsinki, Finland, 1-5 June 2015

[8] DTG Technology (2015). Available at: www.fbgs.com/technology/dtg-technology

[9] Bettini P., Guerreschi E., Sala G., *Development and Experimental Validation of a Numerical Tool for Structural Health and Usage Monitoring*

Systems Based on Chirped Grating Sensors. SENSORS 15, 1321-1341 (2015).

[10] Rostami A., Yazdanpanah-Goharrizi A., *A New Method for Classification and Identification of Complex Fiber Bragg Gratings Using the Genetic Algorithm.* Prog. Electromagn. Res. 75, 329–356 (2007)

[11] Li H.C.H., Herszeberg I., Davis C.E., Mouritz A.P., Galea S.C., *Health Monitoring of marine composite structural joints using fibre optic sensors*, Composite Structures 75; 321-327, (2006)

[12] Herszeberg I. , Mouritz A.P., *Automated characterization of structural disbonds by statistical examination of bond-line strain distribution*, Structural Health Monitoring 5, 83-94 (2006)

[13] K. Raman. *Fiber bragg gratings*. Academic press, 1999.

[14] Balageas, D. Non-Destructive Evaluation of Cooperative Structures (NDECS): A Third Way? *First Asia-Pacific Workshop on SHM*, Yokohama, Japan. 2007.

[15] Balageas D., Fritzen C.P., Güemes A., eds. *Structural health monitoring*. Vol. 493. London: ISTE, 2006.

[16] Raymond M. *Measures*. Structural monitoring with fiber optic technology. Academic, 2001.